SOFT ROBOTICS
Volume 4, Number 2, 2017

DOI: 10.1089/soro.2016.0038

SoRo
Soft Robotics

ORIGINAL ARTICLE

Origami Wheel Transformer: A Variable-Diameter Wheel Drive Robot Using an Origami Structure

Dae-Young Lee,[1,2] Sa-Reum Kim,[1,2] Ji-Suk Kim,[3] Jae-Jun Park,[1] and Kyu-Jin Cho[1,2]

Abstract

A wheel drive mechanism is simple, stable, and efficient, but its mobility in unstructured terrain is seriously limited. Using a deformable wheel is one of the ways to increase the mobility of a wheel drive robot. By changing the radius of its wheels, the robot becomes able to pass over not only high steps but also narrow gaps. In this article, we propose a novel design for a variable-diameter wheel using an origami-based soft robotics design approach. By simply folding a patterned sheet into a wheel shape, a variable-diameter wheel was built without requiring lots of mechanical parts and a complex assembly process. The wheel's diameter can change from 30 to 68 mm, and it is light in weight at about 9.7 g. Although composed of soft materials (fabrics and films), the wheel can bear more than 400 times its weight. The robot was able to change the wheel's radius in response to terrain conditions, allowing it to pass over a 50-mm gap when the wheel is shrunk and a 50-mm step when the wheel is enlarged.

Keywords: origami, deformable wheel, transformable wheel, origami-inspired mechanism, soft origami, origami wheel

Introduction

A MOBILITY OF MOBILE SERVICE robots in an unstructured environment becomes an important performance factor as the scope of applications increases from houses to disaster areas. A wheel mechanism allows simple and stable movement, but its mobility in rugged terrain is seriously limited. To overcome the defects of the wheel mechanisms, various concepts of deformable wheel have been tried. Chen *et al.* proposed the Quattroped, a robot that can reversibly transform its wheels to legs,[1] and Kim *et al.* proposed a wheel transformable robot with a passive rotary leg.[2] Nagatani *et al.* proposed a variable-diameter wheeled robot,[3] and She *et al.* proposed a variable-diameter wheeled robot with a passive leg.[4]

In this article, we propose a novel variable-diameter wheel using an origami-based soft robotics design approach. Soft robots attain infinite degrees of freedom from the soft materials of which they are made (e.g., elastomer and fabric), thereby achieving unique characteristics: dexterous motion, deformability, and adaptability to environments.[5–7] This design concept can be applied to mobile robots, which enables various advantages. Shepherd *et al.* presented a multigait soft robot with highly adaptive movement.[8] Loepfe *et al.* presented a novel movement method—jumping by combustion,[9] and Waynelovich *et al.* presented a dexterous leg system using multichamber leg design.[10] We applied the soft material to create a variable-diameter wheel mechanism.

Using soft materials for a variable-diameter wheel accompanies two advantages—high deformability and ability to absorb impact, but inadequate stiffness and excessive degrees of freedom can impede a wheel's functionality. Our key idea is to overcome these deficiencies by making the wheel structure from a soft material where an origami pattern can be applied, which reduces the material's excessive degrees of freedom and increases the structure's stiffness. Origami is the art of paper folding. The innate characteristics of origami are derived from its metamorphic nature; a single sheet of paper can be turned into numerous three-dimensional (3D) shapes depending on how it is folded.[11] The unique characteristics of origami have made it an attractive solution for many engineering problems, from architectural designs

[1]Department of Mechanical and Aerospace Engineering, Seoul National University, Seoul, Korea.
[2]Seoul National University Institute of Advanced Machines and Design, Seoul National University, Seoul, Korea.
[3]Agency for Defense Development, Daejeon, Korea.

to robot fabrication via microelectromechanical systems (MEMS).[12–14] Martinez *et al.* used an origami concept to build a soft robotic mechanism by focusing on the morphological behavior of the origami structure.[15]

We will focus on the mechanical characteristics of origami. By patterning a rigid material on a soft material, it is possible to construct a substrate with flexible regions (folding parts) that provide high deformability and rigid regions (facets) that regulate excessive degrees of freedom and increase stiffness, for improved functionality. We used two types of facets—a rigid one and a flexible one—to adjust the wheel structure's degrees of freedom. Instead of simply separating the facets and fold lines as in a conventional origami design, our method uses facets of different stiffnesses, allowing high design flexibility.

Although the proposed design loses one major advantage of soft robots, high adaptability provided by soft material's high degrees of freedom, it provides three key advantages. First, the structure can be built without lots of mechanical parts or a complex assembly process. A single sheet replaces most parts, and a folding part generates each joint. This reduces not only the fabrication cost for each part but also the time required for assembly. Second, an origami structure can have high stiffness and impact capacity compared to its weight. In complex kinematic structures, the local distortion of links and joint alignments strongly affects how a structure moves. However, an origami structure is composed of compliant folding parts and facets, so the whole structure can perform as a shock absorber. Also, a specially organized origami structure such as a honeycomb greatly increases the effective stiffness of the whole structure. Third, an origami structure is scalable. The structure generates a joint by folding and this reduces friction between the links. Finally, the simplified assembly process made possible by using origami structures reduces the difficulty of assembling small-scale parts.

A previous study has presented a deformable wheel based on a soft material.[16] This wheel can generate various motions, but it requires many actuators and is insufficiently stiff. To reduce the number of actuators needed, we built a robot with origami wheels that use a space sail folding pattern.[17] However, this pattern did not provide enough stiffness, so we used a waterbomb pattern to solve the problem.[18,19] The proposed wheel design was adopted to the mobile robot runs on multiple terrains, ''SNU-MAX,'' winner of first *RoboSoft Grand Challenge*.[20]

This article describes an improved version of the robot and provides a comprehensive analysis of the wheel structure. The kinematic model of the wheel structure proposed in the article allows the analysis and optimization of the design parameters. For the robot design, special components such as temporarily assembled hubs and a flexible shaft are used to improve the robot's form factor and the performance. Also, a new fabrication method is proposed to utilize laser machining for the patterning and mesh fabric to reinforce the adhesive force. The Experiments section presents the performance of the wheel and the robot. The fabricated wheel structure weighs about 9.7 g and can endure more than 400 times its weight, and the robot can change the wheel diameter from 30 to 68 mm, allowing it to pass through a 50-mm gap and climb a 50-mm step.

Design of the Variable-Diameter Wheel

Wheel pattern design

The origami pattern for the variable-diameter wheel structure derives from the spherical waterbomb tessellated pattern. This structure has been used in several other applications because of its unique characteristic.[21–23] The entire shape of the waterbomb structure can be changed from a prolate spheroid to an oblate spheroid, and therefore, the structure's variable circular circumference can be used as a diameter-changing mechanism (Fig. 1). In the wheel design, eight units are repeated in a circumferential direction to make a circular rim shape, and three units are repeated in the axial direction to make the support structure (Fig. 2a).

The design of the connection between the wheel and the wheel shaft is important for stable movement and torque transmission. Movement of the wheel structure causes complex shape changes at its ends. However, these ends need to maintain a specific configuration to permit the wheel structure to be connected to a shaft. To solve this problem, a bridging pattern was added to the beginning and end of the waterbomb folding pattern to create a new shape at both ends of the folded structure, as shown in Figure 2b. The bridge is assembled by attaching the overlapped facets and allows the ends of the modified wheel structure to remain perpendicular to the shaft and to maintain their configuration even when the wheel shape is deformed, so that the ends can work as joints that connect the wheel to a hub component. Figure 3 shows attachment regions with a hub component that is compatible with the ends of the modified wheel structure.

The final shape of the wheel is shown in Figure 4. The wheel structure has three parts. The hub part makes a connection between the wheel shaft and the wheel, maintaining

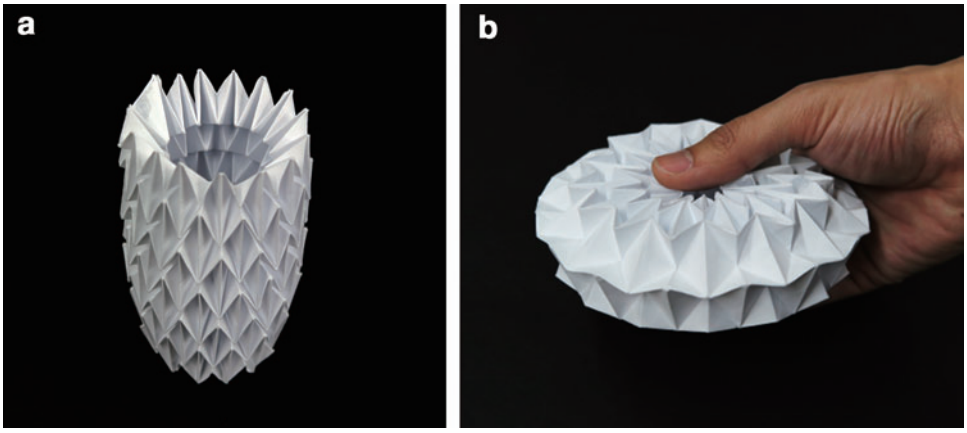

FIG. 1. Spherical waterbomb tessellated pattern. The shape changes from a prolate spheroid **(a)** to an oblate spheroid **(b)** in response to external force. Color images available online at www.liebertpub.com/soro

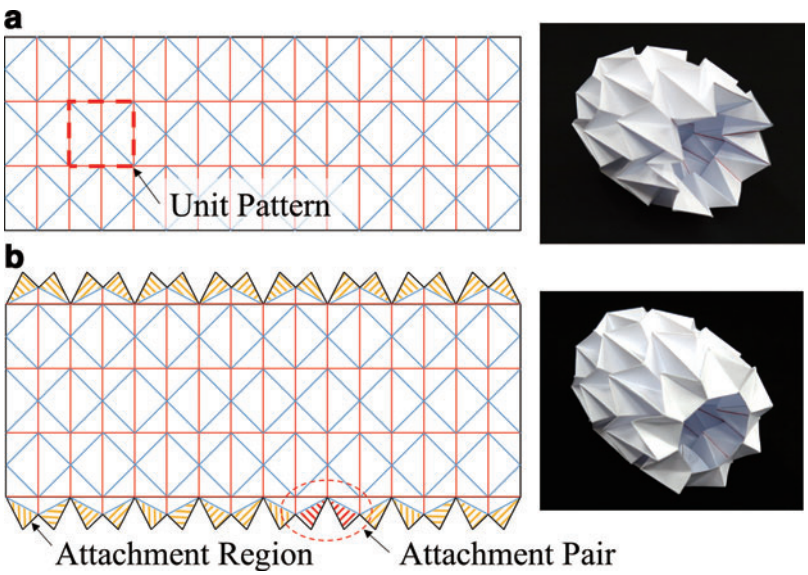

FIG. 2. Pattern and folded shape of conventional 3×8 waterbomb pattern **(a)**, and modified pattern with added bridge components **(b)**. Hatched area in **(b)** presents attachment regions. A blue line signifies a valley fold, and a red line signifies a mountain fold. Color images available online at www.liebertpub.com/soro

the wheel in a circular shape. The support part can vary the wheel's diameter by changes in its slope angle. The rim part forms the main body of the wheel, and it can be extended or shrunk to vary the wheel's diameter.

Kinematic analysis of wheel structure

Technically, the origami structure cannot follow ideal rigid body kinematics. A fold line cannot be an ideal line and should have a specific width. Also, facets may bend owing to compliance of the material from which the structure is made. In other words, the structure can move regardless of its kinematic mobility. Although the kinematics of the structure cannot perfectly constrain the structure, kinematic analysis is still important because kinematics determines the moving direction of the structure, and lack of kinematic mobility hinders movement. To ensure mobility and improve deformation performance, kinematic analysis of the wheel structure was conducted based on the assumption that the folding part is an ideal revolute joint.

The wheel structure analysis was conducted in three steps. First, the variables were specified and the constraints were derived from the geometry of each part. These variables and constraint equations determine the configuration of each part. Next, the symmetry constraints for maintaining the circular shape of the wheel were added. In the last step, the constraints for assembling of each part were derived.

The symbol rules for points and vectors on the structure are shown in Figure 5. Because it has circular symmetry, the entire structure can be represented by the position of a point on two lines, which were named as line A and line B. A subscript indicates the position of points and their order.

Because repeated number of the pattern is specified, only three length parameters of the wheel remain (Fig. 6): l_h, the half-length of the hub plate; l_t, the length of the deformation trigger bar, and l_u, the half-length of the unit pattern. Figure 4a shows the coordinates, points, and variables for representing the wheel hub. The reference frame $\Sigma_{\mathcal{H}}: o_{\mathcal{H}} - x_{\mathcal{H}} y_{\mathcal{H}} z_{\mathcal{H}}$ is used to present the position vector for the points on the wheel hub. The configuration of the wheel hub is determined by two variables, $\theta_{\mathcal{H}1}$ and $\theta_{\mathcal{H}2}$.

From the defined parameters, the position vectors of the points of the wheel hub can be derived as follows:

$$ {}^{\mathcal{H}}\mathbf{p}_{A_{\mathcal{H}1}} = \begin{bmatrix} l_h \\ 0 \\ 0 \end{bmatrix} \tag{1} $$

$$ {}^{\mathcal{H}}\mathbf{p}_{A_{\mathcal{H}2}} = \begin{bmatrix} l_t \cos\theta_{\mathcal{H}1} + l_h \\ 0 \\ l_t \sin\theta_{\mathcal{H}1} \end{bmatrix} \tag{2} $$

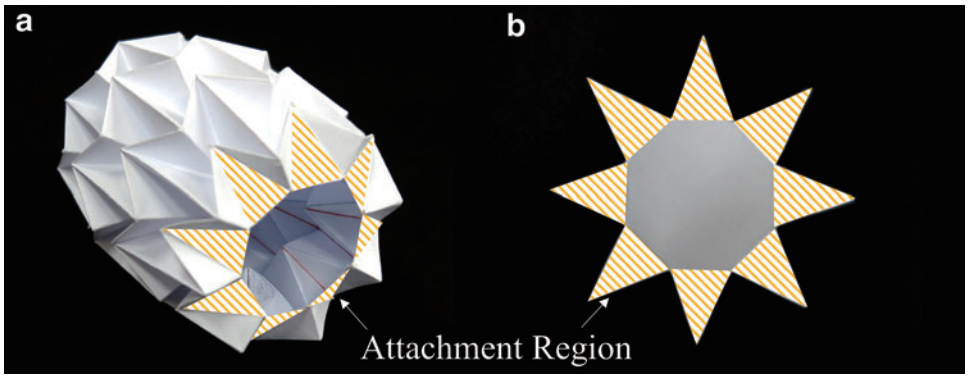

FIG. 3. The folded wheel shape with added bridge components **(a)** and hub component **(b)**. Hatched area presents attachment regions. Color images available online at www.liebertpub.com/soro

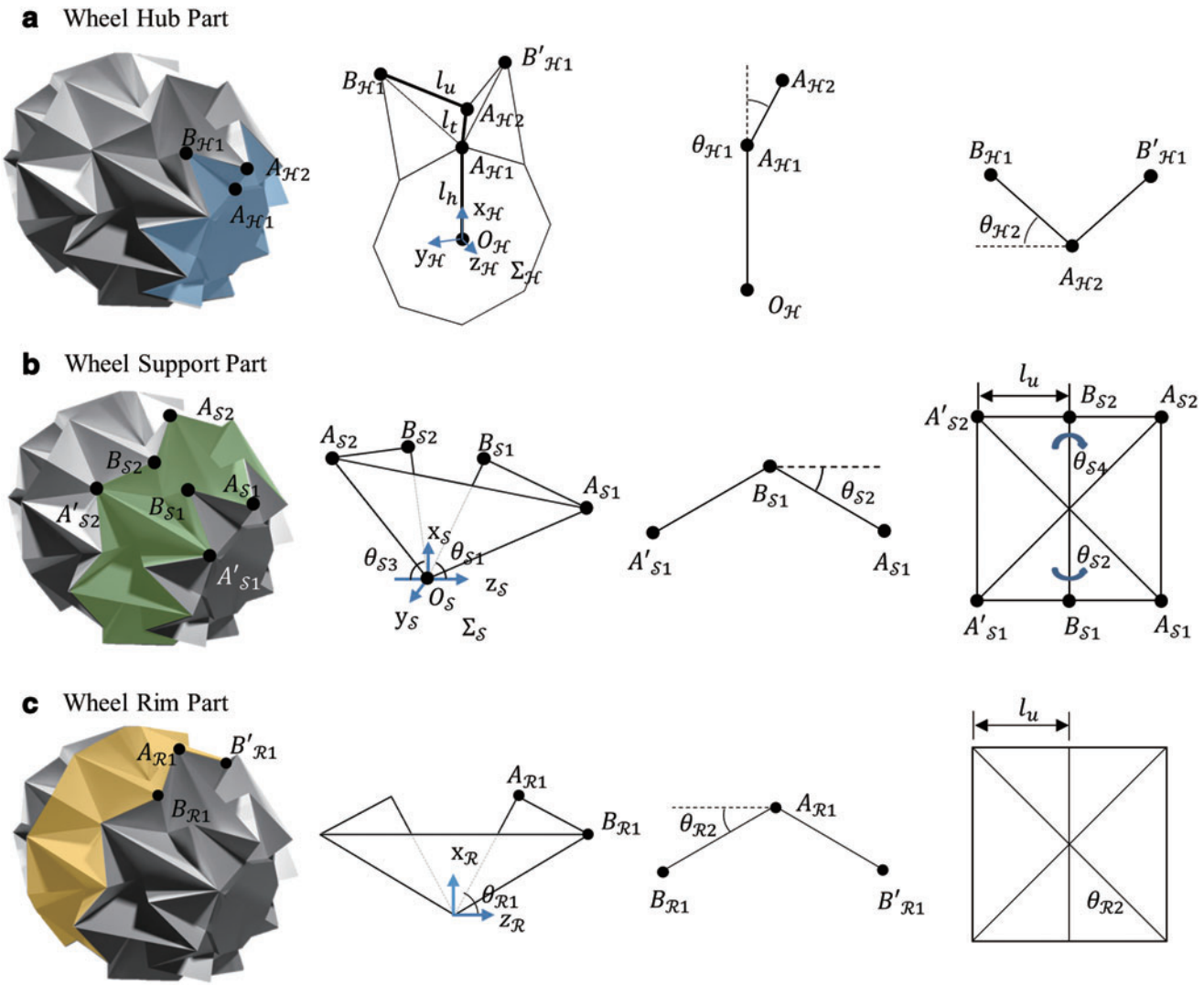

FIG. 4. Coordinates, points, and variables for representing the wheel hub part **(a)**, the wheel support part **(b)**, and the wheel rim part **(c)**. The configuration of the wheel hub is determined by variables θ_{x1} and θ_{x2}, the configuration of the wheel support is determined by variables θ_{s1}, θ_{s2}, θ_{s3}, and θ_{s4}, and the configuration of the wheel rim is determined by variables θ_{R1} and θ_{R2}. Color images available online at www.liebertpub.com/soro

$$ {}^{\mathcal{H}}\mathbf{p}_{B_{\mathcal{H}1}} = \begin{bmatrix} l_t \cos\theta_{\mathcal{H}1} + l_u \sin\theta_{\mathcal{H}1} \sin\theta_{\mathcal{H}2} + l_h \\ l_u \cos\theta_{\mathcal{H}2} \\ l_t \sin\theta_{\mathcal{H}1} - l_u \cos\theta_{\mathcal{H}1} \sin\theta_{\mathcal{H}2} \end{bmatrix} \quad (3) $$

To satisfy wheel symmetry, point $B_{\mathcal{H}1}$ should be on the symmetry constraint line (Fig. 7a). The wheel has eight repeated unit patterns in the circumferential direction, so the slope angle should be $\frac{\pi}{8}$, but in the equation, we keep it as n for generality. Theoretically, n can be any number greater than or equal to three. However, it can change the structural characteristics such as deformation ratio and stiffness. We will discuss this issue in the Discussion section.

From the symmetry constraint, a constraint equation is derived as follows:

$$ \frac{{}^{\mathcal{H}}y_{B_{\mathcal{H}1}}}{{}^{\mathcal{H}}x_{B_{\mathcal{H}1}}} = \tan\frac{\pi}{n} = \frac{l_u \cos\theta_{\mathcal{H}2}}{l_t \cos\theta_{\mathcal{H}1} + l_u \sin\theta_{\mathcal{H}1} \sin\theta_{\mathcal{H}2} + l_h} \quad (4) $$

$$ \textbf{Const. 1} \quad \tan\frac{\pi}{n}\left(\frac{l_t \cos\theta_{\mathcal{H}1} + l_h}{l_u} + \sin\theta_{\mathcal{H}1}\sin\theta_{\mathcal{H}2}\right) - \cos\theta_{\mathcal{H}2} = 0 \quad (5) $$

The analysis of the wheel support is conducted similarly to the wheel hub analysis. The reference frame $\Sigma_{\mathcal{S}}: o_{\mathcal{S}} - x_{\mathcal{S}}y_{\mathcal{S}}z_{\mathcal{S}}$ is used to present the position vectors of the points on the wheel support. Figure 4b shows the coordinates, points, and variables for representing the wheel support. The wheel support has a geometrical constraint because the length of the line $\overline{A_{\mathcal{S}1}A_{\mathcal{S}2}}$ should have a certain value. Equation (6) shows the constraint:

$$ {}^{\mathcal{S}}\mathbf{p}_{A_{s1}} - {}^{\mathcal{S}}\mathbf{p}_{A_{s2}} = 2l_u \quad (6) $$

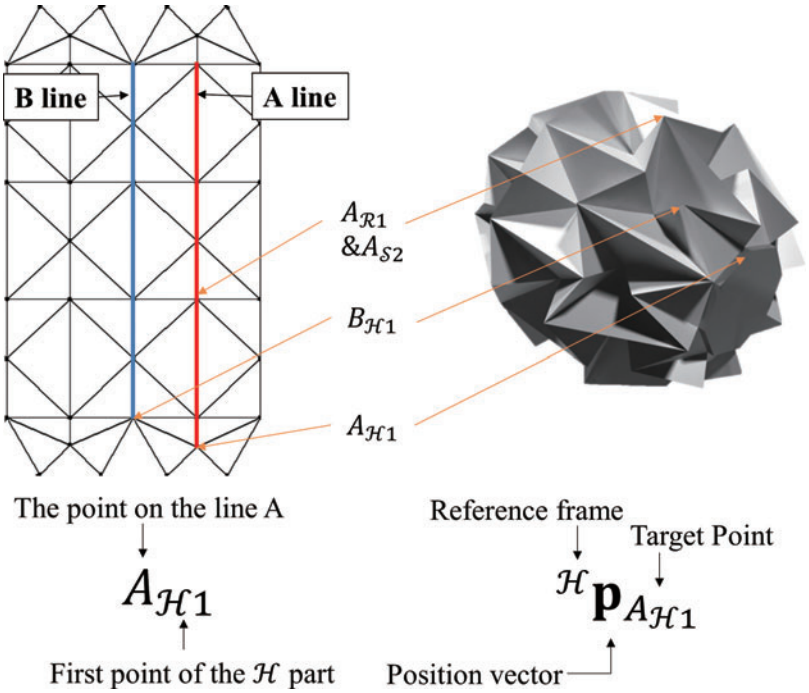

FIG. 5. Graphical view of symbol rules for structure analysis. Because of its symmetry, the entire structure can be represented by the position of a point on two lines [18]. Color images available online at www.liebertpub.com/soro

From the position vector:

$$ {}^{\mathcal{S}}\mathbf{p}_{A_{\mathcal{S}1}} = \begin{bmatrix} l_u(\sin\theta_{\mathcal{S}1} - \cos\theta_{\mathcal{S}1}\sin\theta_{\mathcal{S}2}) \\ -l_u\cos\theta_{\mathcal{S}2} \\ l_u(\cos\theta_{\mathcal{S}1} + \sin\theta_{\mathcal{S}1}\sin\theta_{\mathcal{S}2}) \end{bmatrix} \tag{7} $$

$$ {}^{\mathcal{S}}\mathbf{p}_{A_{s2}} = \begin{bmatrix} l_u(\sin\theta_{\mathcal{S}3} - \cos\theta_{\mathcal{S}3}\sin\theta_{\mathcal{S}4}) \\ -l_u\cos\theta_{\mathcal{S}4} \\ -l_u(\cos\theta_{\mathcal{S}3} + \sin\theta_{\mathcal{S}3}\sin\theta_{\mathcal{S}4}) \end{bmatrix} \tag{8} $$

By substituting Equations (7) and (8) for Equation (6), the constraint equation is derived as

$$ \begin{aligned} \textbf{Const. 2:}\ & (\sin\theta_{\mathcal{S}2} + \sin\theta_{\mathcal{S}4})\sin(\theta_{\mathcal{S}1} + \theta_{\mathcal{S}3}) \\ & + (1 - \sin\theta_{\mathcal{S}2}\sin\theta_{\mathcal{S}4})\cos(\theta_{\mathcal{S}1} + \theta_{\mathcal{S}3}) \\ & - \cos\theta_{\mathcal{S}2}\cos\theta_{\mathcal{S}4} = 0 \end{aligned} \tag{9} $$

Similar to the wheel hub, the wheel support needs to satisfy the symmetry constraint. Figure 7b graphically shows the constraint. The height variable $\rho_{\mathcal{S}}$ is added to represent the height of the wheel support reference frame from the wheel center, and the new reference frame $\Sigma_{\mathcal{S}'}$ is defined.

Points $A_{\mathcal{S}1}$ and $A_{\mathcal{S}2}$ should be on the symmetry constraint line so that their position vector satisfies the constraint.

$$ {}^{\mathcal{S}'}\mathbf{p}_{A_{\mathcal{S}1}} = \begin{bmatrix} \rho_{\mathcal{S}} + l_u(\sin\theta_{\mathcal{S}1} - \cos\theta_{\mathcal{S}1}\sin\theta_{\mathcal{S}2}) \\ -l_u\cos\theta_{\mathcal{S}2} \\ l_u(\cos\theta_{\mathcal{S}1} + \sin\theta_{\mathcal{S}1}\sin\theta_{\mathcal{S}2}) \end{bmatrix} \tag{10} $$

$$ {}^{\mathcal{S}'}\mathbf{p}_{A_{s2}} = \begin{bmatrix} \rho_{\mathcal{S}} + l_u(\sin\theta_{\mathcal{S}3} - \cos\theta_{\mathcal{S}3}\sin\theta_{\mathcal{S}4}) \\ -l_u\cos\theta_{\mathcal{S}4} \\ -l_u(\cos\theta_{\mathcal{S}3} + \sin\theta_{\mathcal{S}3}\sin\theta_{\mathcal{S}4}) \end{bmatrix} \tag{11} $$

$$ \begin{aligned} \textbf{Const. 3:}\ & (\rho_{\mathcal{S}} + l_u(\sin\theta_{\mathcal{S}1} - \cos\theta_{\mathcal{S}1}\sin\theta_{\mathcal{S}2}))\tan\frac{\pi}{n} \\ & - l_u\cos\theta_{\mathcal{S}2} = 0 \end{aligned} \tag{12} $$

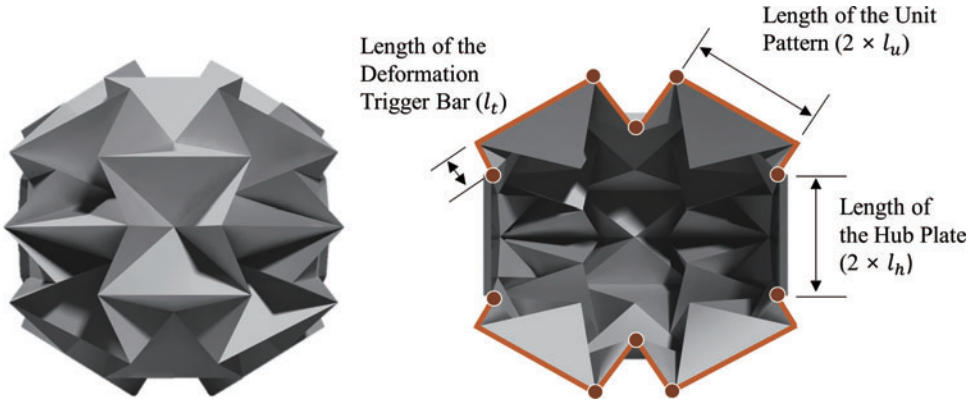

FIG. 6. Design parameters for the wheel. Three length parameters determine the wheel design because the number of patterns is specified [18]. Color images available online at www.liebertpub.com/soro

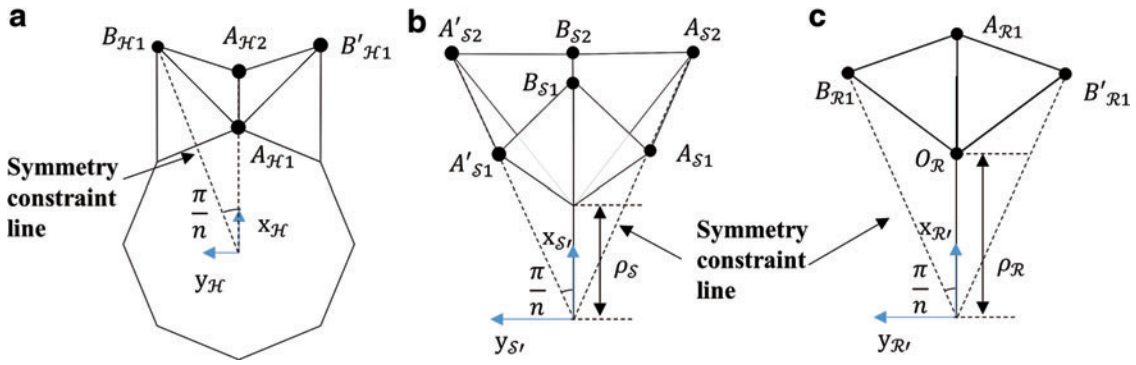

FIG. 7. Symmetry constraint line of the wheel hub part **(a)**, the wheel support part **(b)**, and the wheel rim part **(c)**. Color images available online at www.liebertpub.com/soro

$$\textbf{Const. 4.}\ (\rho_{\mathcal{S}} + l_u(\sin\theta_{\mathcal{S}3} - \cos\theta_{\mathcal{S}3}\sin\theta_{\mathcal{S}4}))\tan\frac{\pi}{n} - l_u\cos\theta_{\mathcal{S}4} = 0 \quad (13)$$

The geometry of the wheel rim is similar to that of the wheel support, but it is symmetrical about the $x_{\mathcal{R}}y_{\mathcal{R}}$ plane. Only two variables, $\theta_{\mathcal{R}1}$, $\theta_{\mathcal{R}2}$, are required to determine the configuration of the part. The reference frame $\Sigma_{\mathcal{R}} : o_{\mathcal{R}} - x_{\mathcal{R}}y_{\mathcal{R}}z_{\mathcal{R}}$ and the variables $\theta_{\mathcal{R}1}$, $\theta_{\mathcal{R}2}$ of the wheel rim are graphically presented in Figure 4c.

From the geometrical constraint, the z position of point $B_{\mathcal{R}1}$ should equal l_u. The vector presentation of point $B_{\mathcal{R}1}$ is

$${}^{\mathcal{R}}\mathbf{p}_{B_{\mathcal{R}1}} = \begin{bmatrix} l_u(\sin\theta_{\mathcal{R}1} - \cos\theta_{\mathcal{R}1}\sin\theta_{\mathcal{R}2}) \\ l_u\cos\theta_{\mathcal{R}2} \\ l_u(\cos\theta_{\mathcal{R}1} + \sin\theta_{\mathcal{R}1}\sin\theta_{\mathcal{R}2}) \end{bmatrix} \quad (14)$$

Therefore the constraint is

$$\textbf{Const. 5}\ (\cos\theta_{\mathcal{R}1} + \sin\theta_{\mathcal{R}1}\sin\theta_{\mathcal{R}2}) = 1 \quad (15)$$

Similar to the wheel support, the height variable $\rho_{\mathcal{R}}$ and new reference frame $\Sigma_{\mathcal{R}'}$ are introduced to make the symmetry constraint. Because point $B_{\mathcal{R}1}$ should be on the symmetry constraint line as the wheel hub and the wheel support (Fig. 7c), the constraint equation can be derived from the position vector:

$${}^{\mathcal{R}'}\mathbf{p}_{B_{\mathcal{R}1}} = \begin{bmatrix} \rho_{\mathcal{R}} + l_u(\sin\theta_{\mathcal{R}1} - \cos\theta_{\mathcal{R}1}\sin\theta_{\mathcal{R}2}) \\ l_u\cos\theta_{\mathcal{R}2} \\ l_u(\cos\theta_{\mathcal{R}1} + \sin\theta_{\mathcal{R}1}\sin\theta_{\mathcal{R}2}) \end{bmatrix} \quad (16)$$

$$\textbf{Const. 6}\ \{\rho_{\mathcal{R}} + l_u(\sin\theta_{\mathcal{R}1} - \cos\theta_{\mathcal{R}1}\sin\theta_{\mathcal{R}2})\}\tan\frac{\pi}{n} - l_u\cos\theta_{\mathcal{R}2} = 0 \quad (17)$$

Because the three parts are assembled, new constraint equations should be derived from the assembly. To assemble all parts, a general coordinate named ''wheel frame,'' $\Sigma_{\mathcal{W}}$, is introduced as shown in Figure 8. New variables, $\eta_{\mathcal{S}}$, $\eta_{\mathcal{H}}$ representing the relative position of $\Sigma_{\mathcal{S}}$, $\Sigma_{\mathcal{H}}$ in the z-direction,

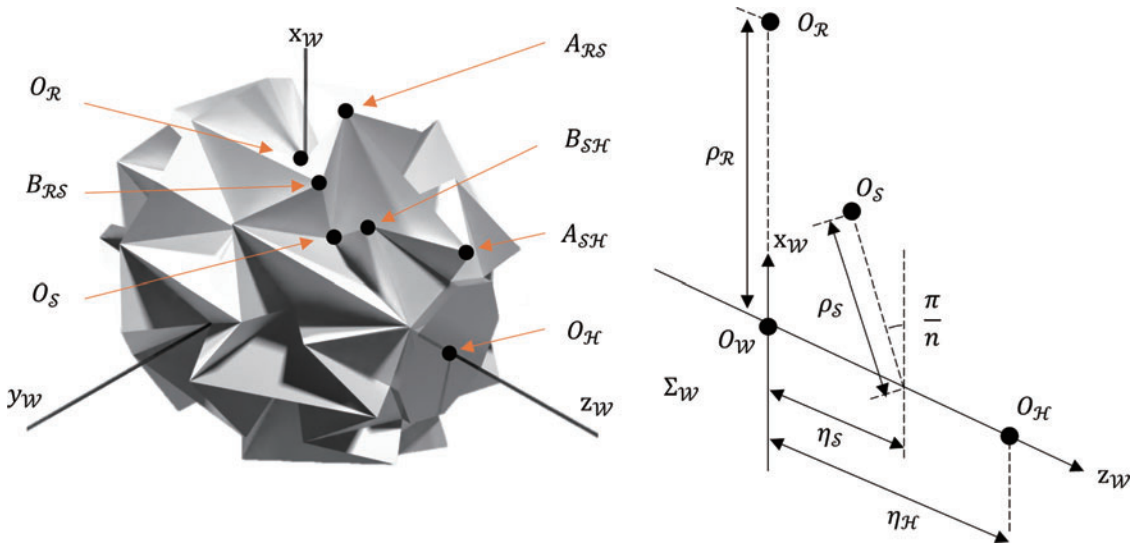

FIG. 8. General coordinate Σ_w for the parts assembly. The variables η_s and η_x represent the relative position of Σ_{s1}, Σ_x in the z-direction [18]. Color images available online at www.liebertpub.com/soro

are used. For convenience, all coordinates are presented in cylindrical form, and the symbol $\widehat{\mathrm{p}}$ is used to indicate the point vector in a cylindrical coordinate.

To assemble the wheel support and the wheel hub, point $A_{\mathcal{S}1}$ on the wheel support should be at the same position as point $A_{\mathcal{H}2}$ on the hub. Also, points $B_{\mathcal{S}1}$ and $B_{\mathcal{H}1}$ should be at the same positions. Similarly, points $A_{\mathcal{R}1}$and $A_{\mathcal{S}2}$, and points $B_{\mathcal{R}1}$ and $B_{\mathcal{S}2}$, respectively, should be at the same positions for assembly of the wheel rim and wheel support.

Using Equation (12), the radius term of the vector ${}^{\mathcal{W}}\widehat{\mathbf{p}}_{A_{\mathcal{S}1}}$ in Equation (18) is simplified, and therefore, the position vectors of $A_{\mathcal{S}1}$ and $A_{\mathcal{H}2}$ in the cylindrical coordinate are presented as

$$\mathcal{W}\widehat{\mathbf{p}}_{A_{\mathcal{S}1}} = \begin{bmatrix} l_u \cos\theta_{\mathcal{S}2} / \sin\frac{\pi}{n} \\ 0 \\ \eta_{\mathcal{S}} + l_u \cos\theta_{\mathcal{S}1} + l_u \sin\theta_{\mathcal{S}1} \sin\theta_{\mathcal{S}2} \end{bmatrix} \tag{18}$$

$$\mathcal{W}\widehat{\mathbf{p}}_{A_{\mathcal{H}2}} = \begin{bmatrix} l_h + l_t \cos\theta_{\mathcal{H}1} \\ 0 \\ \eta_{\mathcal{H}} + l_t \sin\theta_{\mathcal{H}1} \end{bmatrix} \tag{19}$$

The derived constraint equations are

$$\rho_{A_{\mathcal{SH}}} = l_u \cos\theta_{\mathcal{S}2} / \sin\frac{\pi}{n} = l_h + l_t \cos\theta_{\mathcal{H}1} \tag{20}$$

$$\eta_{A_{\mathcal{S}}\mathcal{H}} = \eta_{\mathcal{S}} + l_u \cos\theta_{s1} + l_u \sin\theta_{\mathcal{S}1} \sin\theta_{\mathcal{S}2} = \eta_{\mathcal{H}} + l_t \sin\theta_{\mathcal{H}1} \tag{21}$$

where $A_{\mathcal{SH}}$ is the assembly point in line A of the wheel support and the wheel hub (Fig. 8).

Similarly, the position vectors $B_{\mathcal{S}1}$ and $B_{\mathcal{H}1}$ in the cylindrical coordinate are presented as

$$\mathcal{W}\widehat{\mathbf{p}}_{B_{\mathcal{S}1}} = \begin{bmatrix} \rho_{\mathcal{S}} + l_u \sin\theta_{\mathcal{S}1} \\ \pi/n \\ \eta_{\mathcal{S}} + l_u \cos\theta_{\mathcal{S}1} \end{bmatrix} \tag{22}$$

$$\mathcal{W}\widehat{p}_{B_{\mathcal{H}1}} = \begin{bmatrix} l_u \cos\theta_{\mathcal{H}2} / \sin\frac{\pi}{n} \\ \pi/n \\ \eta_{\mathcal{H}} + l_t \sin\theta_{\mathcal{H}1} - l_u \sin\theta_{\mathcal{H}2} \cos\theta_{\mathcal{H}1} \end{bmatrix} \tag{23}$$

So the derived constraint equations are

$$\rho_{B_{\mathcal{SH}}} = \rho_{\mathcal{S}} + l_u \sin\theta_{\mathcal{S}1} = l_u \cos\theta_{\mathcal{H}2} / \sin\frac{\pi}{n} \tag{24}$$

$$\begin{aligned} \eta_{B_{\mathcal{SH}}} = \eta_{\mathcal{S}} + l_u \cos\theta_{\mathcal{S}1} = \eta_{\mathcal{H}} + l_t \sin\theta_{\mathcal{H}1} \\ - l_u \sin\theta_{\mathcal{H}2} \cos\theta_{\mathcal{H}1} \end{aligned} \tag{25}$$

The length between points $A_{\mathcal{H}2}$ and $B_{\mathcal{H}1}$ and the length between points $A_{\mathcal{S}1}$ and $B_{\mathcal{S}1}$ should be equal, so there is redundancy in the constraint equations. From this constraint, Equation (26) with Equations (5) and (12) can be summarized as Equation (27).

$$\eta_{A_{\mathcal{SH}}} - \eta_{B_{\mathcal{SH}}} = l_u \cos\theta_{\mathcal{H}1} \sin\theta_{\mathcal{H}2} = l_u \sin\theta_{\mathcal{S}1} \sin\theta_{\mathcal{S}2} \tag{26}$$

$$\eta_{A_{\mathcal{SH}}} - \eta_{B_{\mathcal{SH}}} = \sqrt{l_u^2 - \rho_{A_{\mathcal{SH}}}^2 - \rho_{B_{\mathcal{SH}}}^2 + 2\rho_{A_{\mathcal{SH}}} \rho_{B_{\mathcal{SH}}} \cos\frac{\pi}{n}} \tag{27}$$

The equations show that the value of $\eta_{A_{\mathcal{SH}}} - \eta_{B_{\mathcal{SH}}}$ can be determined by the values of $\rho_{A_{\mathcal{SH}}}$ and $\rho_{B_{\mathcal{SH}}}$, which means that the constraint equations for these three values determine the other value. If the constraint equation for $\rho_{A_{\mathcal{SH}}}$, $\rho_{B_{\mathcal{SH}}}$, and $\eta_{A_{\mathcal{SH}}}$ is satisfied, the value of $\eta_{B_{\mathcal{SH}}}$ is consequentially constrained. Therefore, four constraint equations can be reduced to three:

$$\textbf{Const. 7:}\ l_u \cos\theta_{\mathcal{S}2} / \sin\frac{\pi}{n} - l_h - l_t \cos\theta_{\mathcal{H}1} = 0 \tag{28}$$

$$\begin{aligned} \textbf{Const. 8:}\ \eta_{\mathcal{S}} + l_u \cos\theta_{\mathcal{S}1} + l_u \sin\theta_{\mathcal{S}1} \sin\theta_{\mathcal{S}2} \\ - (\eta_{\mathcal{H}} + l_t \sin\theta_{\mathcal{H}1}) = 0 \end{aligned} \tag{29}$$

$$\textbf{Const. 9:}\ \rho_{\mathcal{S}} + l_u \sin\theta_{\mathcal{S}1} - l_u \cos\theta_{\mathcal{H}2} / \sin\frac{\pi}{n} = 0 \tag{30}$$

Similarly, the point vectors and the constraint equations for points $A_{\mathcal{R}1}$, $A_{\mathcal{S}2}$, $B_{\mathcal{R}1}$, and $B_{\mathcal{S}2}$ can be achieved as follows:

$${}^{\mathcal{W}}\widehat{\mathbf{p}}_{A_{\mathcal{R}1}} = \begin{bmatrix} \rho_{\mathcal{R}} + l_u \sin\theta_{\mathcal{R}1} \\ 0 \\ l_u \cos\theta_{\mathcal{R}1} \end{bmatrix} \tag{31}$$

$${}^{\mathcal{W}}\widehat{\mathbf{p}}_{A_{\mathcal{S}2}} = \begin{bmatrix} l_u \cos\theta_{\mathcal{S}4} / \sin\frac{\pi}{n} \\ 0 \\ \eta_{\mathcal{S}} - l_u \cos\theta_{\mathcal{S}3} - l_u \sin\theta_{\mathcal{S}3} \sin\theta_{\mathcal{S}4} \end{bmatrix} \tag{32}$$

$${}^{\mathcal{W}}\widehat{\mathbf{p}}_{B_{\mathcal{R}1}} = \begin{bmatrix} l_u \cos\theta_{\mathcal{R}2} / \sin\frac{\pi}{n} \\ \pi/n \\ l_u \cos\theta_{\mathcal{R}1} + l_u \sin\theta_{\mathcal{R}1} \sin\theta_{\mathcal{R}2} \end{bmatrix} \tag{33}$$

$${}^{\mathcal{W}}\widehat{\mathbf{p}}_{B_{\mathcal{S}2}} = \begin{bmatrix} \rho_{\mathcal{S}} + l_u \sin\theta_{\mathcal{S}3} \\ \pi/n \\ \eta_{\mathcal{S}} - l_u \cos\theta_{\mathcal{S}3} \end{bmatrix} \tag{34}$$

$$\rho_{A_{\mathcal{RS}}} = \rho_{\mathcal{R}} + l_u \sin\theta_{\mathcal{R}1} = l_u \cos\theta_{\mathcal{S}4} / \sin\frac{\pi}{n} \tag{35}$$

$$\eta_{A_{\mathcal{RS}}} = l_u \cos\theta_{\mathcal{R}1} = \eta_{\mathcal{S}} - l_u \cos\theta_{\mathcal{S}3} - l_u \sin\theta_{\mathcal{S}3} \sin\theta_{\mathcal{S}4} \tag{36}$$

$$\rho_{B_{\mathcal{RS}}} = l_u \cos\theta_{\mathcal{R}2} / \sin\frac{\pi}{n} = \rho_{\mathcal{S}} + l_u \sin\theta_{\mathcal{S}3} \tag{37}$$

$$\eta_{B_{\mathcal{RS}}} = l_u \cos\theta_{\mathcal{R}1} + l_u \sin\theta_{\mathcal{R}1} \sin\theta_{\mathcal{R}2} = \eta_{\mathcal{S}} - l_u \cos\theta_{\mathcal{S}3} \tag{38}$$

Table 1. Variables Determining Wheel Configuration

	Angle variable	*Position variable*
Wheel hub part	$\theta_{\mathcal{H}1}$, $\theta_{\mathcal{H}2}$	$\eta_{\mathcal{H}}$
Wheel support part	$\theta_{\mathcal{S}1}$, $\theta_{\mathcal{S}2}$, $\theta_{\mathcal{S}3}$, $\theta_{\mathcal{S}4}$	$\rho_{\mathcal{S}}$, $\eta_{\mathcal{S}}$
Wheel rim part	$\theta_{\mathcal{R}1}$, $\theta_{\mathcal{R}2}$	$\rho_{\mathcal{R}}$

$$\textbf{Const. 10}\ \rho_{\mathcal{R}} + l_u \sin\theta_{\mathcal{R}1} - l_u \cos\theta_{\mathcal{S}4}/\sin\frac{\pi}{n} = 0 \quad (39)$$

$$\textbf{Const. 11}\ l_u \cos\theta_{\mathcal{R}2}/\sin\frac{\pi}{n} - (\rho_{\mathcal{S}} + l_u \sin\theta_{\mathcal{S}3}) = 0 \quad (40)$$

$$\textbf{Const. 12}\ l_u \cos\theta_{\mathcal{R}1} + l_u \sin\theta_{\mathcal{R}1}\sin\theta_{\mathcal{R}2} - (\eta_{\mathcal{S}} - l_u \cos\theta_{\mathcal{S}3}) = 0 \quad (41)$$

Overall, 12 variables and 12 constraint equations were derived, and the results are summarized in Tables 1 and 2. The mechanism composed of 12 variables with 12 constraints has zero kinematic degrees of freedom. The manufactured prototype is deformable because its facets are made of compliant material. Nevertheless, material deformation requires high force in the movement of the structure and also causes material failure because of high stress concentration. We will discuss this issue in the next section.

Hybrid pattern design with flexible facets

The proposed structure has an equal number of variables with constraint equations, which leads to zero mobility of the mechanism. This problem can be solved by cutting the material, but that would seriously weaken the structure's robustness. Our solution to this problem is releasing the constraints by using a flexible facet in a specific region. This is simply achieved by increasing the area of the folding part. A small width of the folding part constrains most of the movement of the adjacent facets without revolute joint motion. However, increasing the area of the folding part to a level of the facet allows for much more flexible movement so that the adjacent facets gain extra degrees of freedom. This approach—utilizing both rigid and flexible facets—allows high design flexibility.

The target constraint to be released is the assembly constraint on point $A_{\mathcal{R}}\mathcal{S}$, which is the assembly point in line A between the wheel rim and the wheel support part. This point was chosen to be released because it endures high external force when the wheel contacts the ground owing to its prominent geometry.

Assembly of one point generates two constraint equations. Therefore, releasing the assembly of one point generates two extra degrees of freedom. However, this also breaks the redundancy of the equations, so that the number of the constraints for assembling the wheel rim with the wheel support becomes two not one. As a result, constraint 10 (Eqn. 39) is eliminated, and the total degrees of freedom is changed to one by using a flexible facet.

The modified origami pattern is shown in Figure 9. The wheel is made of two laminated materials, one rigid and one flexible, so that variation of the pattern for the rigid parts creates a flexible facet region. As a result, the total degrees of freedom in the structure could be adjusted to a desirable value. Further information about the material composition of the wheel is presented in the Fabrication section.

Wheel design parameter selection

The wheel structure has three design parameters: length of the unit pattern, length of the hub plate, and length of the deformation trigger bar. The maximum deformation ratio can be achieved by adjusting these parameters.

The length of the unit pattern determines the maximum and minimum diameter of the wheel rim. The wheel rim has three variables—$\rho_{\mathcal{R}}$, $\theta_{\mathcal{R}1}$, and $\theta_{\mathcal{R}2}$—with two constraint Equations (15) and (17). The radius of the wheel—x position of A_{R1}, is

$$^{\mathcal{R}'}\boldsymbol{x}_{A_{R1}} = \rho_{\mathcal{R}} + l_u \sin\theta_{\mathcal{R}1} \quad (42)$$

The optimization problem with the constraints was solved by the MATLAB optimization tool, which reported a maximum

Table 2. Constraints Determining Wheel Configuration

Constraint of wheel hub part	
$\tan\frac{\pi}{n}\left(\frac{l_t\cos\theta_{\mathcal{H}1}+l_h}{l_u} + \sin\theta_{\mathcal{H}1}\sin\theta_{\mathcal{H}2}\right) - \cos\theta_{\mathcal{H}2} = 0$	(5)
Constraint of wheel support part	
$(\sin\theta_{\mathcal{S}2} + \sin\theta_{\mathcal{S}4})\sin(\theta_{\mathcal{S}1}+\theta_{\mathcal{S}3}) + (1 - \sin\theta_{\mathcal{S}2}\sin\theta_{\mathcal{S}4})\cos(\theta_{\mathcal{S}1}+\theta_{\mathcal{S}3}) - \cos\theta_{\mathcal{S}2}\cos\theta_{\mathcal{S}4} = 0$	(9)
$(\rho_{\mathcal{S}} + l_u(\sin\theta_{\mathcal{S}1} - \cos\theta_{\mathcal{S}1}\sin\theta_{\mathcal{S}2}))\tan\frac{\pi}{n} - l_u\cos\theta_{\mathcal{S}2} = 0$	(12)
$(\rho_{\mathcal{S}} + l_u(\sin\theta_{\mathcal{S}3} - \cos\theta_{\mathcal{S}3}\sin\theta_{\mathcal{S}4}))\tan\frac{\pi}{n} - l_u\cos\theta_{\mathcal{S}4} = 0$	(13)
Constraint of wheel rim part	
$(\cos\theta_{\mathcal{R}1} + \sin\theta_{\mathcal{R}1}\sin\theta_{\mathcal{R}2}) = 1$	(15)
$(\rho_{\mathcal{R}} + l_u(\sin\theta_{\mathcal{R}1} - \cos\theta_{\mathcal{R}1}\sin\theta_{\mathcal{R}2}))\tan\frac{\pi}{n} - l_u\cos\theta_{\mathcal{R}2} = 0$	(17)
Constraint of hub support part assembly	
$l_u\cos\theta_{\mathcal{S}2}/\sin\frac{\pi}{n} - l_h + l_t\cos\theta_{\mathcal{H}1} = 0$	(28)
$\eta_{\mathcal{S}} + l_u\cos\theta_{\mathcal{S}1} + l_u\sin\theta_{\mathcal{S}1}\sin\theta_{\mathcal{S}2} - (\eta_{\mathcal{H}} + l_t\sin\theta_{\mathcal{H}1}) = 0$	(29)
$\rho_{\mathcal{S}} + l_u\sin\theta_{\mathcal{S}1} - l_u\cos\theta_{\mathcal{H}2}/\sin\frac{\pi}{n} = 0$	(30)
Constraint of support—rim part assembly	
$\rho_{\mathcal{R}} + l_u\sin\theta_{\mathcal{R}1} - l_u\cos\theta_{\mathcal{S}4}/\sin\frac{\pi}{n} = 0$	(39)
$l_u\cos\theta_{\mathcal{R}2}/\sin\frac{\pi}{n} - (\rho_{\mathcal{S}} + l_u\sin\theta_{\mathcal{S}3}) = 0$	(40)
$l_u\cos\theta_{\mathcal{R}1} + l_u\sin\theta_{\mathcal{R}1}\sin\theta_{\mathcal{R}2} - (\eta_{\mathcal{S}} - l_u\cos\theta_{\mathcal{S}3}) = 0$	(41)

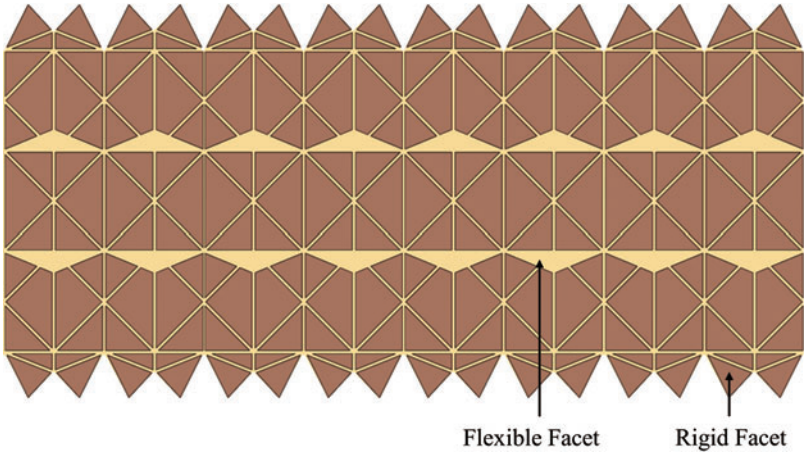

FIG. 9. The final pattern of variable-diameter wheel. The patterning on the flexible material overly constrains movement, but adding flexible facets adjusts the degrees of freedom. Color images available online at www.liebertpub.com/soro

value as 2.56 l_u and a minimum value as l_u. Based on these results, the ideal maximum deformation ratio is 2.56.

To maximize the deformation ratio, other design parameters—l_h and l_t—should be matched with l_u. The minimum radius of the wheel is the summation of l_h and l_t, and the maximum radius of the wheel is the summation of l_h and 2 l_u. Therefore, to achieve the maximum deformation ratio, Equation (43) should be satisfied. In this article, l_u is 12.5 mm, l_h is 10 mm, and l_t is 4 mm.

$$\frac{l_h + 2l_u}{l_h + l_t} = 2.56 \tag{43}$$

The size of the flexible facet is another important design parameter. Figure 10a shows the schematic diagram of the flexible facet. The position of point A_{S2} is changed because of the flexible facet, and the flexible facet should link the separated points (A_{S2} and $A_{\mathcal{R}1}$). Therefore, if the length of the flexible facet is shorter than the distance between two points, it hinders the movement of the wheel structure. However, an overly long length of the flexible facet may weaken the payload of the wheel.

Figure 10b shows the tendency of the maximum distance to vary as the length of the flexible facet increases. The intersection point represents the optimal length of the flexible facet, which is the minimum length that does not interfere with the movement of the wheel. The coordinate values of the points were computed with MATLAB by solving the derived equations. From the analysis, 4.47 mm of the length of the flexible facet (about 18% of the length of the unit pattern) was chosen as the proper value. The effect of the flexible facet is investigated in the Experiments section.

Robot Design

Wheel deformation and torque transmission mechanism

The diameter of the wheel is varied by changing the length of the wheel in the direction of the axis. To allow for relative motion of the hub, at least one side of the wheel should be adjustable. Moving the outside wheel hub can reduce the applied bending moment on the shaft, but it requires a large internal space to allow the shaft to slide with the stroke. According to the wheel dimension selection in the previous section, each shaft requires at least 40 mm of internal space in a robot body.

To reduce the required internal space, we replaced the rigid shaft with a flexible one. The flexible shaft is connected to the

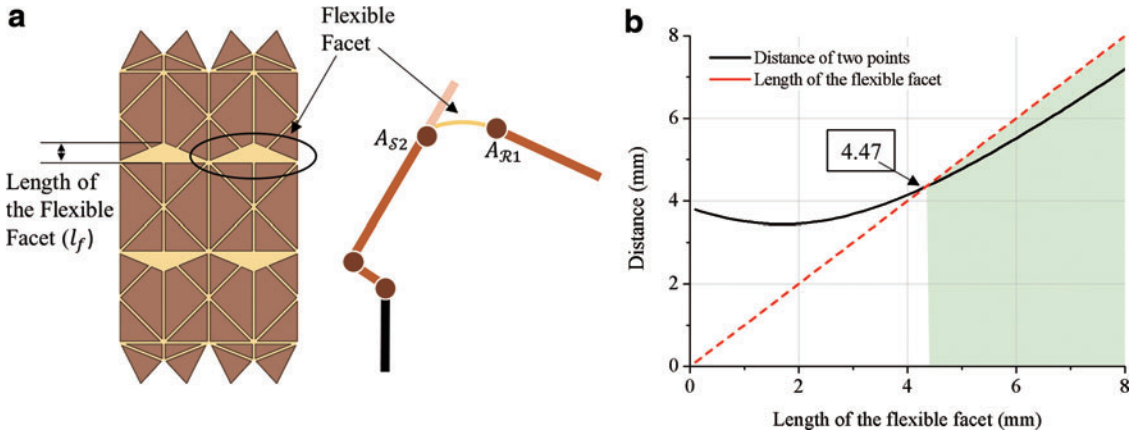

FIG. 10. Schematic diagram of the flexible facet **(a)** and tendency of maximum distance to vary as length of the flexible facet increases **(b)**. A value of 4.47 mm of the length of the flexible facet (about 18% of the length of the unit pattern) has been chosen. Color images available online at www.liebertpub.com/soro

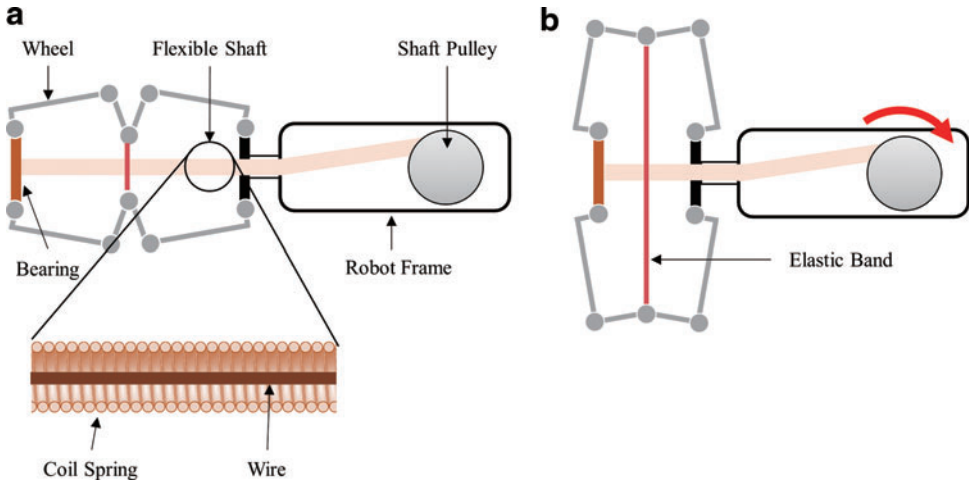

FIG. 11. Schematic of the wheel deformation mechanism using a flexible shaft. The coil spring allows the shaft to be wound up on the pulley and prevents twisting. The internal wire prevents extension of the coil spring. Color images available online at www.liebertpub.com/soro

outside hub via a bearing, so the shaft can pull the outside hub when the shaft pulley winds it up (Fig. 11). To ensure low resistance force during winding, a material with low bending stiffness is preferred. However, a low-stiffness material is susceptible to twisting when the wheel rotates.

To solve the problem, we used an anisotropic structure that has low bending stiffness and high torsional stiffness: a coil spring with a wire in its center (Fig. 11a). Coil springs have low bending stiffness and relatively high torsional stiffness, so the shaft can be wound up on the pulley without twisting. The wire prevents extension of the coil spring. The elastic band encircles the wheel to recover the original shape when the shaft tension is released (Fig. 11b).

Another issue with using a flexible shaft is the potential for wheel axis misalignment. This happens when the flexible shaft structure cannot hold the position of the outside hub. In the shrunk state, bending the wheel axis causes only a small variation in the contact height of the wheel with the ground, but in the enlarged state, the problem became significant. To prevent this problem, a specially designed hub structure was built (Fig. 12). The outer hubs prevent over-deformation of the wheel. The inner hubs are assembled at the enlarged state, and in this configuration they function as a shaft. These components create a stable wheel configuration.

For the path of the flexible shaft, the driving motors transmit rotation torque to the wheel via gears. Figure 13a shows the detailed design and overall view of the robot. The robot has two deformable wheels on both sides and a carriage tail for the electronics and batteries. The tail structure is also necessary for obstacle climbing. For driving the wheel, 1.5 W DC motors (1224E 256:1; FAULHABER) were used, and for wheel deformation, the identical motor with an encoder was used. Figure 13b shows the assembly view and components for the deformation mechanism. The body structure was separated into two parts for assembly.

Wheel grouser design

Using a wheel grouser increases the robot's ability to overcome obstacles by changing the shape of the wheel to function like a rotary leg. The grouser should be assembled robustly to the wheel, folded at the shrunk state, and deployed in the enlarged state. To satisfy these conditions, the wheel grousers were attached to facets of the wheel support (Fig. 14).

Since the contact between the wheel and the ground mainly occurs through the grouser, fixing the grouser and designing the contact face can significantly affect the driving performance. Because polyethylene terephthalate (PET) material

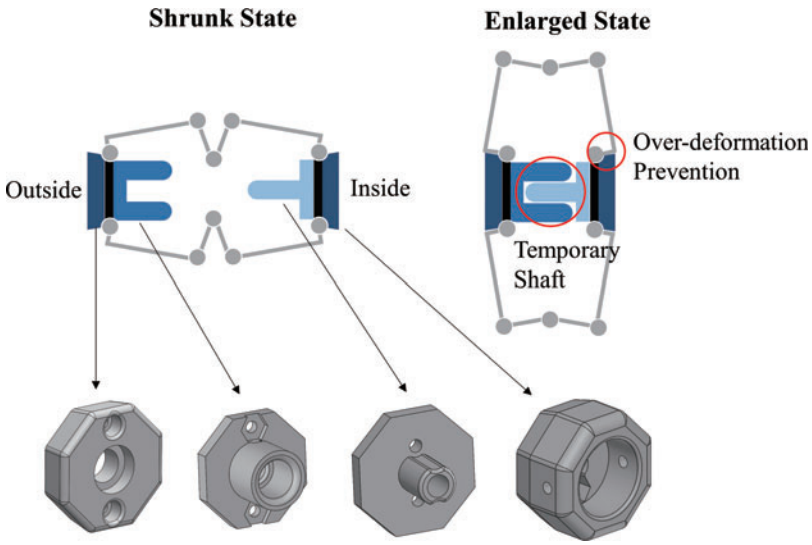

FIG. 12. Wheel hub design for the axis misalignment problem. Color images available online at www.liebertpub.com/soro

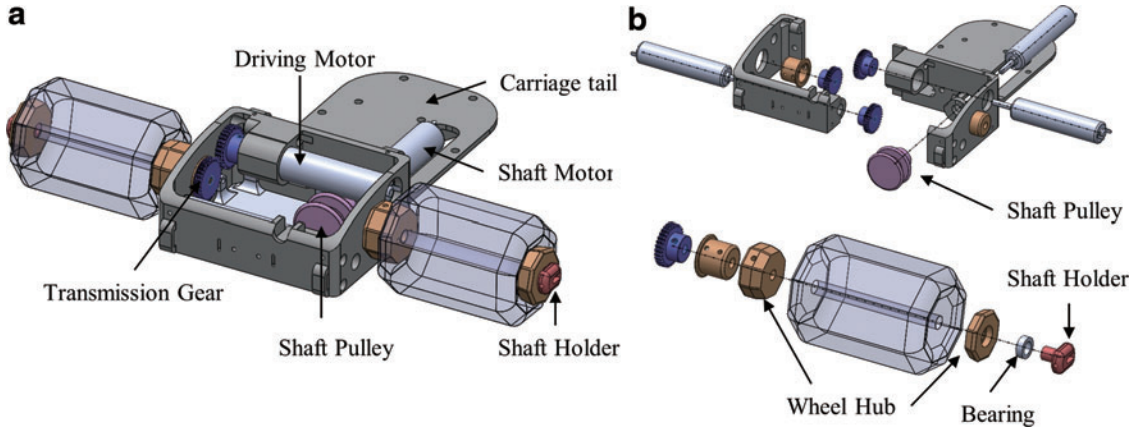

FIG. 13. Overall view of the robot **(a)**, and assembly view and components of the wheel deformation mechanism **(b)**. Color images available online at www.liebertpub.com/soro

was used for the facet, a chemical adhesive would not provide enough adhesive force. Mechanical joining methods such as bolts or riveting are also not appropriate for thin origami structures. We attached the grouser with a stapler and adhesive tape. Figure 14 shows the grouser design. The grouser was made with a multimaterial 3D printer, which allowed to design the grouser to have a rubber-like region for stapling and increasing the friction of the contact face.

The proposed method provides a stable binding, but it has a limitation on scalability and requires a complex assembling process. In addition, since the ground contact point of the grouser should move when the wheel is deformed, the high friction force between the grouser and the ground can interfere with the deformation. A material property of the grouser can also be an important factor when the robot is heavy. Therefore, use of the grouser should be determined according to the kind of application. The grouser is suitable for two-wheel drive, small and light mobile robots. Large and heavy robots in the form of a four-wheel drive do not necessarily require the grouser.

Electronics and interface

Figure 15 presents the control schematic for the robot. The control interface was built with a commercial WIFI camera module and an Arduino Nano controller. The WIFI camera module (P5206-2; HanJin Data) can be connected with a smartphone application (offered by HanJin Data) via WIFI, so the user can see real-time video and also send a command. The WIFI camera module provides user commands via UART communication using a preset data protocol. An Arduino Nano was used for the main control unit. Arduino Nano interprets user commands from the WIFI camera module and combines them with an encoder signal to control the motors.

Fabrication

Wheel fabrication

For wheel fabrication, multimaterial patterning was adopted rather than single-material patterning. The basic concept of multimaterial origami design is to utilize the difference in stiffness between the facet and the folding part. The material for the facets should be laser machinable, and the material for the folding part should be highly flexible and resistant to fatigue. A PET film (100 μm; Kolami) with a thermal adhesive on one side was chosen for the facets, and a plain weave mesh fabric was used for the folding part. The mesh fabric is so pliable that it cannot only bend the entire wheel shape easily but also be folded thousands of times. In addition, the thermal adhesive permeates the mesh, which reinforces its adhesive strength.

Figure 16 illustrates the fabrication process. First, the PET film is attached to a weakly adhesive polyamide film (CT-1065; Coretec), which is used to hold the PET film during

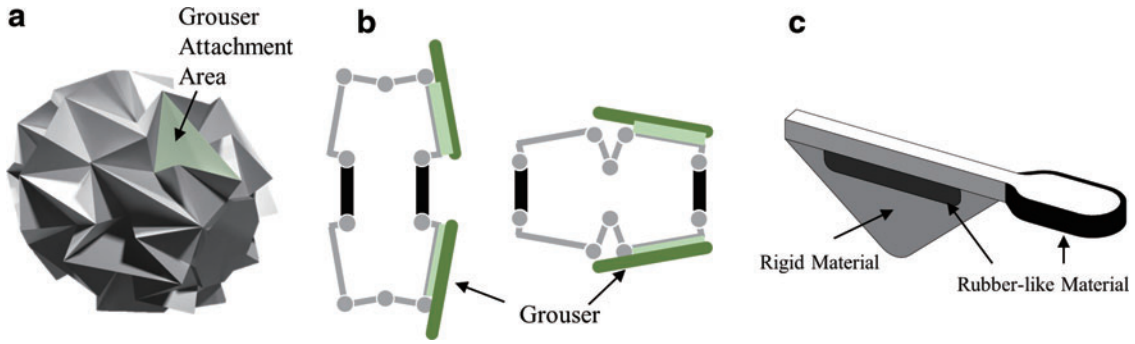

FIG. 14. Grouser attachment area **(a)**, schematic of grouser deployment **(b)**, and design of the wheel grouser **(c)**. Color images available online at www.liebertpub.com/soro

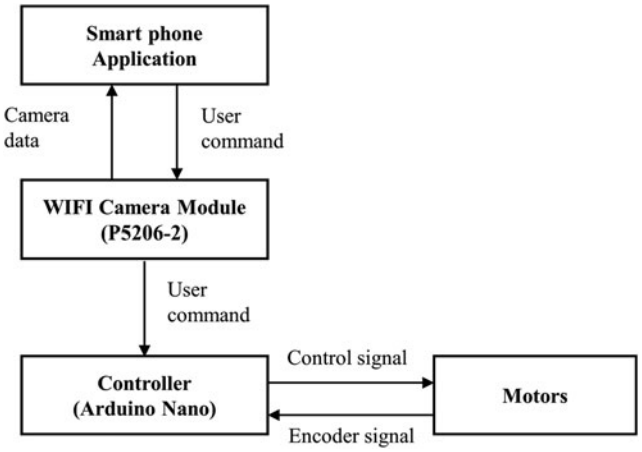

FIG. 15. Control interface block diagram.

laser machining (VLS 3.5; Universal Laser System) (a, b). After the unnecessary part of the PET has been removed (c), the mesh fabric is sandwiched between the two processed PET films (d). Because the PET film remains adhered to the polyamide film, it is easy to align the two intricate patterns by hand on a backlight glass (e). In the next step, the sandwiched layers are put into a hydraulic hot press (QM900A; QME-SYS) at 5 MPa at a temperature of 110°C for 5 min and then cooled for 1 h at room temperature (f). During this process, the resin on the PET film melts and infiltrates the fabric, causing the PET to stick so strongly to the mesh that the facets are hard to peel off the fabric despite many foldings. The polyamide film is then removed from both sides of the quenched substrate (g) and a double-sided adhesive (5316K; Coretec Co.) is pasted to a few parts of the pattern and to the hubs so that they can be fashioned into a wheel shape (h). Before folding up the pattern, grousers are attached using staplers (i). The grousers are 3D printed (Object 260; Stratasys Ltd.) using multimaterials (VeroWhite and Tango-Black; Stratasys Ltd.). The wheel pattern is then folded and

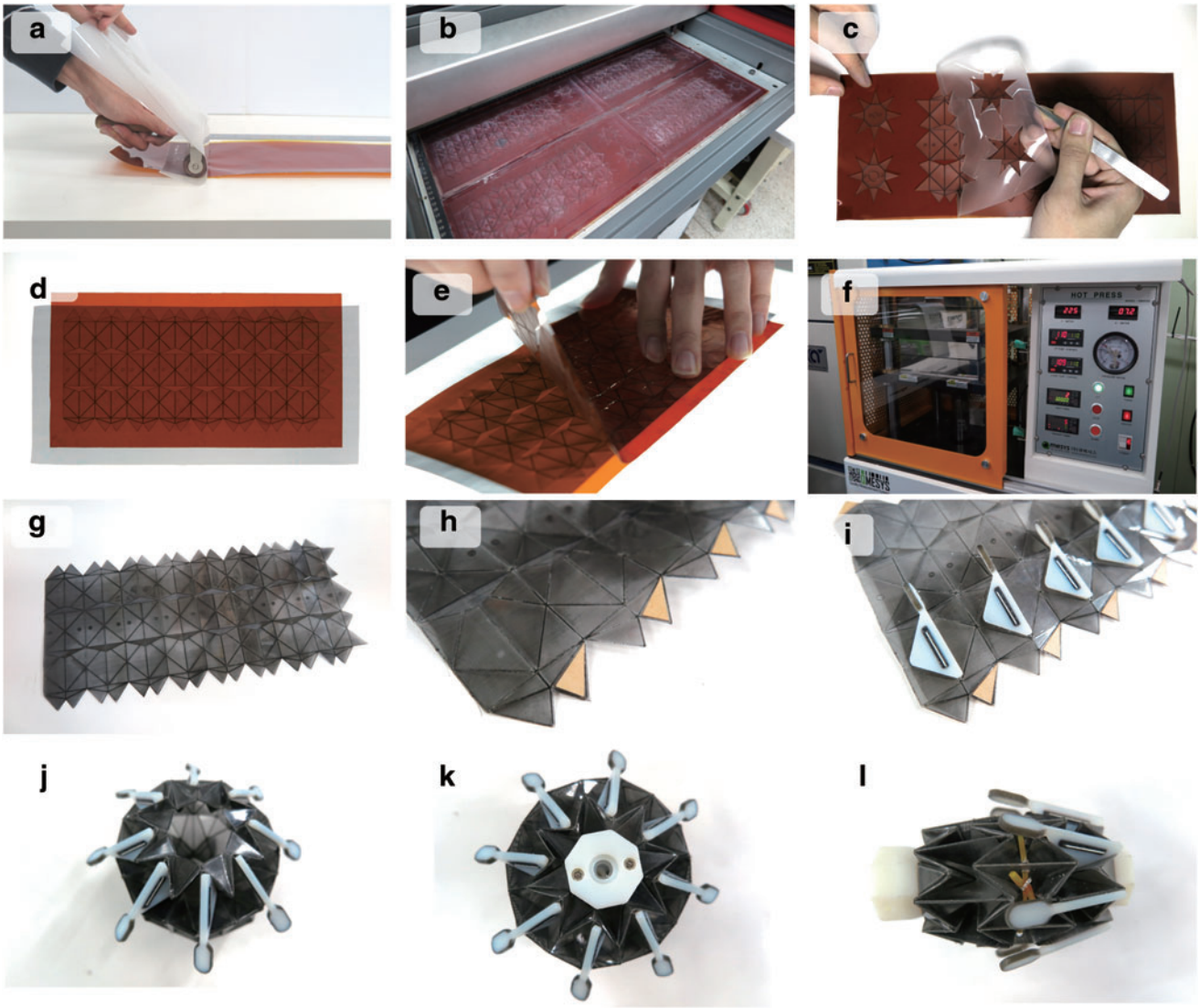

FIG. 16. Wheel fabrication process **(a–l)**. Color images available online at www.liebertpub.com/soro

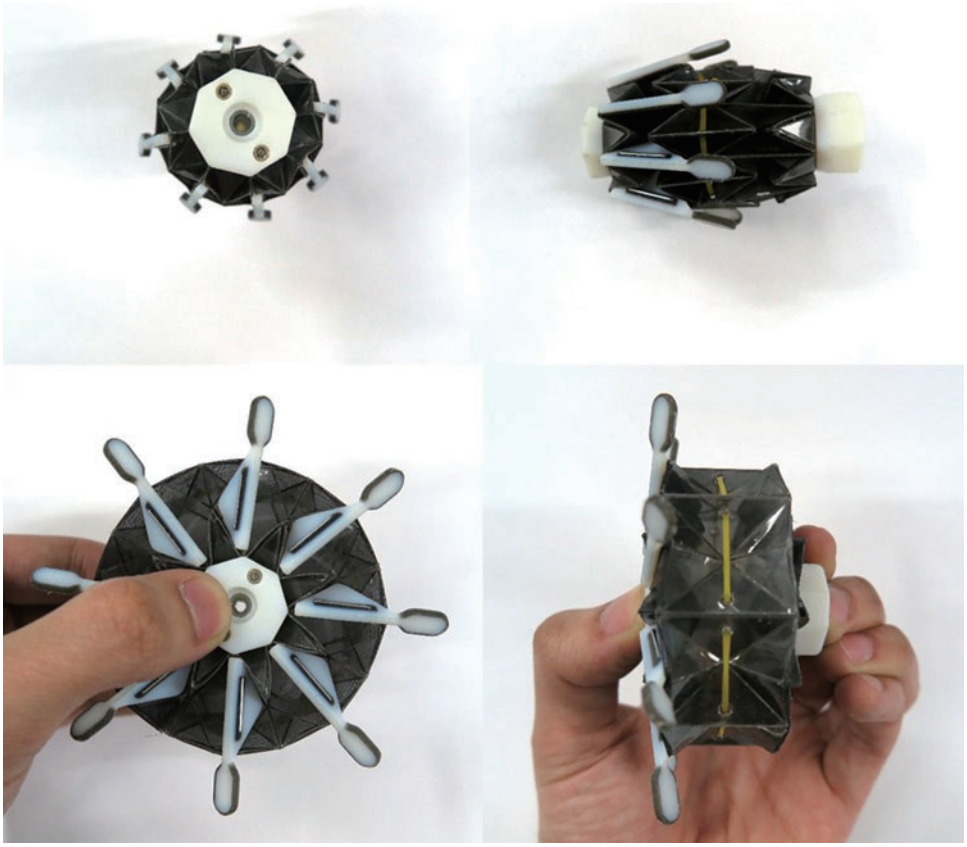

FIG. 17. Wheel fabrication results. Color images available online at www.liebertpub.com/soro

assembled with the hub components (j, k). Finally, a rubber band is wrapped around the wheel in the circumferential direction to apply restoring force after folding (l).

Figure 17 shows the final fabricated wheel. The wheel weighs about 9.7 g with the hub components and 4.7 g without the hub components.

Robot fabrication

All structural components of the robot were fabricated with a 3D printer (Objet 260; Stratasys Ltd.). The communication module, cooling fan, and battery for the controller were placed on the head side, and the main controller and battery for the motors were placed on the carriage tail (Fig. 18). A PET cover was placed on the robot body to protect body components. Figure 18 shows the final robot, which weighs 278 g with batteries.

Experiments

Wheel deformation characteristics

Although the mechanism can move with zero kinematic mobility because of the compliance of the materials, the effect of the flexible facet on wheel performance is considerable. In this section, two performance factors were defined and the effect of the flexible facet was investigated.

The first performance factor is related to the energy required for deformation. A soft robot is composed of a soft and elastic material, so the transmission of a soft robot also

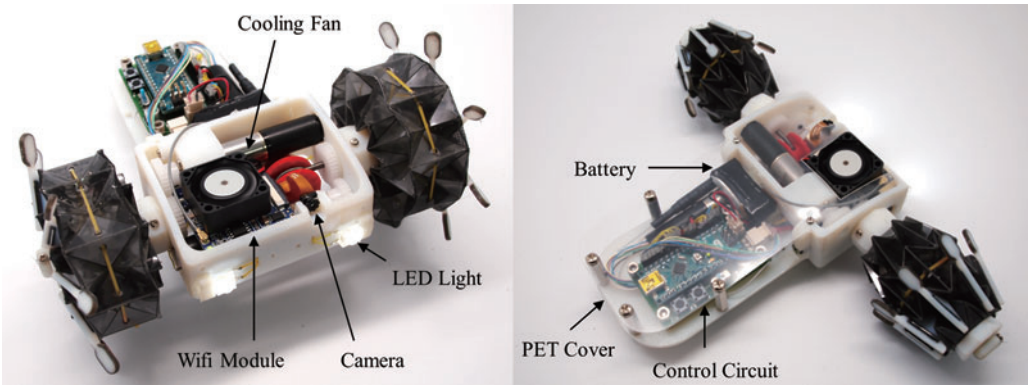

FIG. 18. Final assembled robot. Color images available online at www.liebertpub.com/soro

contains softness. Movement of the mechanism is induced by material deformation and increases the internal energy. Therefore, output movement per input energy can be an important performance factor for the robot. To investigate this, we introduced a performance factor named ''deformation cost'' that represents the required energy per unit output movement. In this case, the output movement is variation of the diameter of the wheel, and the input energy is the pushing force of the wheel hub. The deformation cost factor usually shows a nonlinear response, so the average value was used. The overall input energy was calculated by integrating the pushing force by the displacement from the initial state to the maximally enlarged state and dividing it by the total diameter variation.

The second performance factor is related to sustainability of the structure. The materials used to make soft robots usually have a large elastic region and low stiffness, which causes considerable deformation in response to an applied force. Therefore, both structural stiffness and maximum payload in a target direction are important performance factors, especially when an application needs to endure high force, such as a wheel. Force was applied in a radial direction, and initial structure stiffness (in 5% linearity) and maximum payload were measured.

For the experiments, four types of specimens were prepared. Different types of specimens had different ratios of the flexible facet γ_f (0%, 6%, 18%, and 30%), and the other wheel dimensions were the same as those specified in the Wheel design parameter selection section. Each specimen represents the wheel without flexible facet (0%), with small flexible facet (6%), with theoretically appropriate flexible facet (18%), and with excessive flexible facet (30%).

Figure 19a shows the experimental setup to measure the force for the wheel diameter variation. The wheel was pushed in the direction of the axis by a tensile tester (RB302; Unitech) at a constant speed of 20 mm/min, and the pusher connected to the load cell measured the axial force at a collection speed of 3 Hz.

Figure 20 shows a force–displacement profile for wheel deformation (a) and deformation cost (b). Four copies of each type of specimen are prepared, and all experiments are repeated twice. Both graphs present a ±1 standard deviation. Theoretically, the deformation cost should be saturated at 18%, but the stiffness of the flexible facet causes a consistent decrease in the deformation cost. The expectation comes from the assumption that the facets have infinite stiffness and the flexible part has zero stiffness, and therefore, the results cannot be perfectly matched with the theoretical expectation. Still, it is possible to extract some characteristics of the flexible facet from the results.

First, the flexible facet dramatically reduces the deformation cost, which can be interpreted to mean that the flexible facet reduces distortion of the material. Second, the flexible facet also reduces variation of the deformation cost. High variations in the results derive from the constrained movement of the mechanism. Therefore, low standard deviation can be interpreted as an indication that the mechanism has mobility. Third, the specimen without the flexible facet has bistability, which causes a dramatic decrease in the force profile. The support part of the wheel without a flexible facet cannot move freely and is snapped to the other side when deformation exceeds a specific boundary.

Figure 19b shows the experimental setup for measuring the maximum wheel payload. Each wheel specimen was placed with the shaft in a fixed configuration that maintained the distance between the two hubs at 45 mm, and both ends of the shaft were fixed to the linear guide. The wheel was pushed at a constant speed of 20 mm/min in the radial direction (y-direction in this setup) by the tensile tester (RB302; Unitech) through the shaft connected to the linear guide, which minimized friction force during pushing. The load cell collected the force data during pushing with 3 Hz, and the maximum payload that the specimens could sustain before breaking was measured.

Figure 21 shows the results of the payload test. Four copies of each type of specimen are prepared, and all experiments are not repeated because of structural failure. Both graphs present ±1 standard deviation. The maximum payload was measured at the point when the wheel supports collapsed. When the specimen had no flexible facets, the wheel had high instability and easily collapsed to one side. These specimens showed low maximum payload and initial stiffness with high standard deviation compared to other specimens even though they had the highest deformation cost. As the length of the

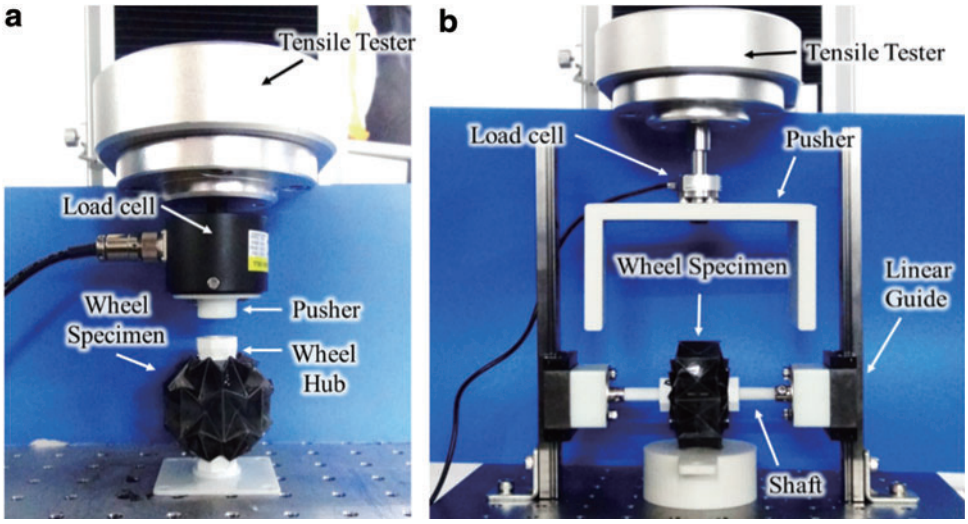

FIG. 19. Experimental setup for the wheel deformation **(a)** and the wheel payload test **(b)**. Color images available online at www.liebertpub.com/soro

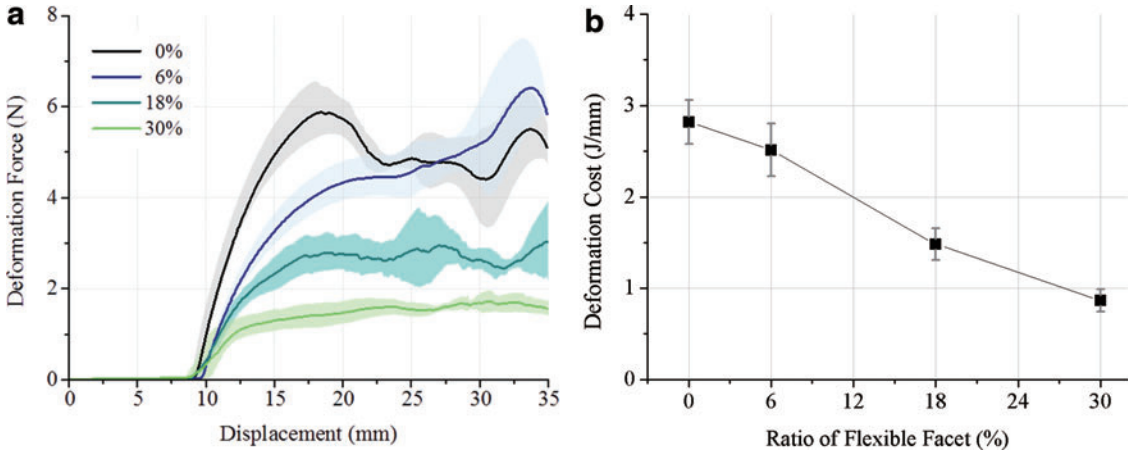

FIG. 20. Experimental results of the wheel diameter variation. The graph **(a)** is a force–displacement profile for wheel deformation and the graph **(b)** shows deformation cost. The area in graph **(a)** presents a ±1 standard deviation. The existence of flexible facets dramatically reduces the deformation cost and standard deviation. Color images available online at www.liebertpub.com/soro

flexible facet increased, the wheel became stable and the maximum payload and initial stiffness also became high, but large flexible facets cannot hold the structure firmly and make the wheel easy to collapse. In the robot, 18% of the flexible facets are used, which shows about 41 N of the maximum payload, which is more than 400 times the weight of the wheel structure.

Another topic we want to discuss is unpredictable payload performance of the wheel in large compression displacement. All specimens were collapsed at a certain point, and it caused a dramatic decrease of the payload. Because of this reason, the standard deviation of all specimens became larger as the displacement increases, and some specimens (the specimens with 18% of flexible facet) show especially irregular behavior. This behavior is due to the limitation of the current fabrication method. The collapse of the specimen is mainly caused by two reasons: material failure (buckling) and delamination. Because all specimens were prepared manually, the quality is hard to be controlled and it caused different failure modes. Thus, the tendency can be estimated, but the accurate analysis is difficult. We will discuss this issue in more detail in the Discussion section.

Robot performance

Figure 22 shows wheel diameter variations for the robot. Theoretical maximum enlarged diameter of the wheel is 70 mm without the grouser and 94 mm with the grouser, and theoretical minimum shrunk diameter of the wheel is 28 and 36 mm with the grouser. Each of the measured enlarged diameters is 68 and 90 mm, and each of the measured shrunk diameters is 28 and 36 mm. The difference between expected and measured values arises from the compliance of the structure. By alternating the wheel diameter between these two states, the robot can climb a 50 mm step and pass over a

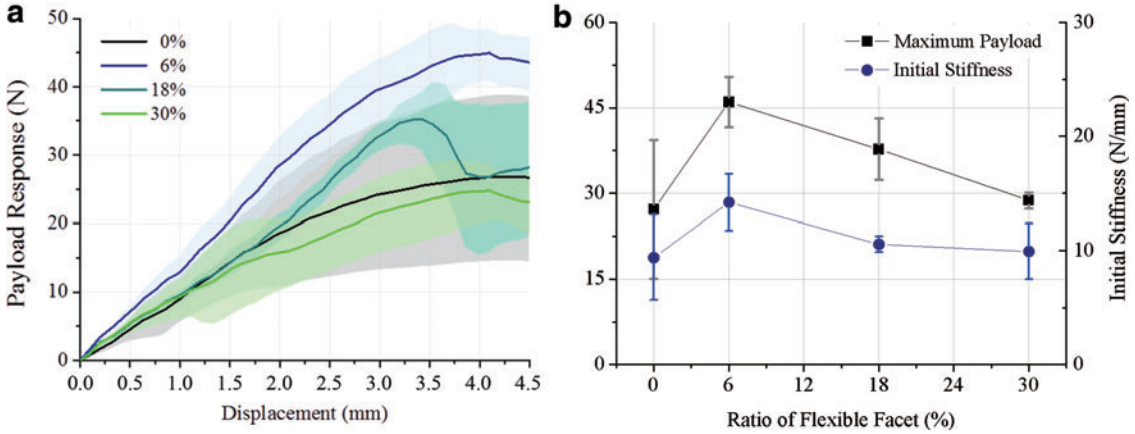

FIG. 21. Experimental results of the wheel payload test. The graph **(a)** shows the force–displacement profile for the wheel payload response and the graph **(b)** shows the maximum payload with initial stiffness (in 5% linearity). As the length of the flexible facet increases, the wheel become stable and maximum payload and initial stiffness also become high, but beyond a certain length a large flexible facet cannot hold the structure and it collapses easily. Color images available online at www.liebertpub.com/soro

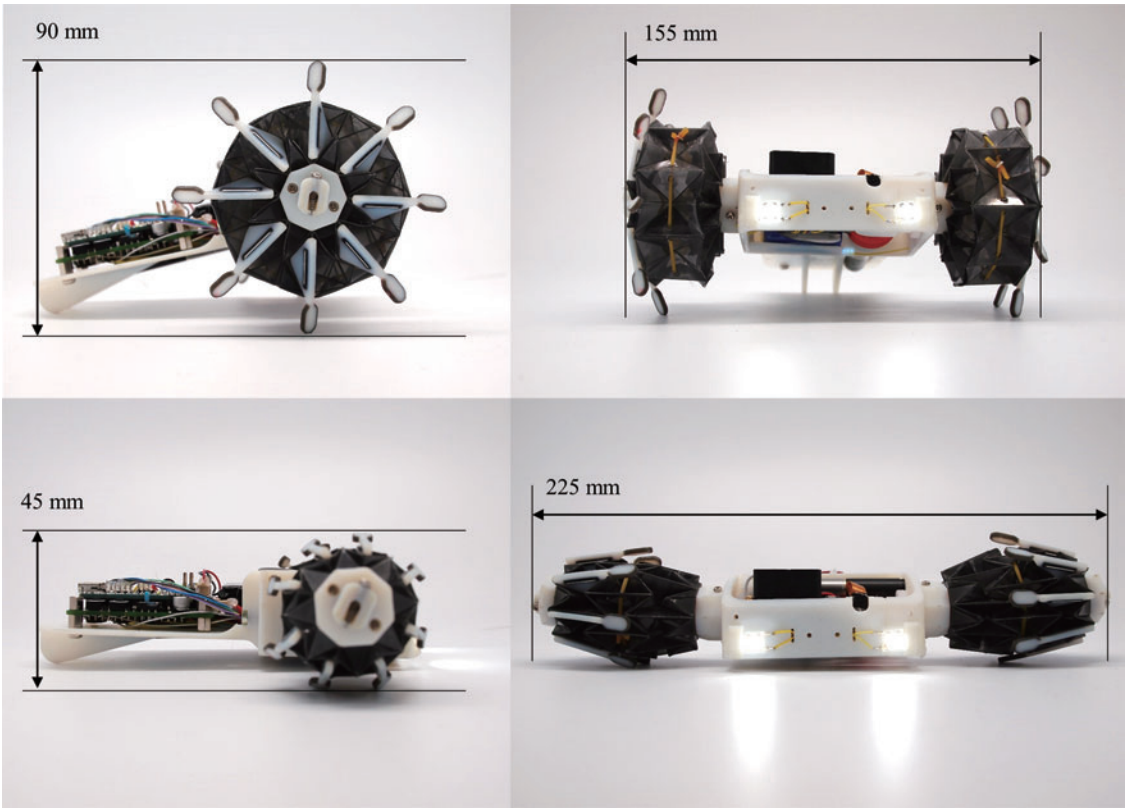

FIG. 22. Wheel diameter variations of the robot. Color images available online at www.liebertpub.com/soro

50 mm gap. Figure 23 shows frames from a videotape of the robot navigating these obstacles.

Discussion

In this article, we suggest a soft robotic application for a deformable wheel. The wheel is an example of a mechanical component that needs to be able to endure high external force. To accomplish this with a soft robotic design approach, we applied origami patterning and tuned the overall behavior of the wheel by segment stiffening. As a result, we developed a lightweight wheel (about 9.7 g) that can deform in size by more than twice its original diameter and deliver a relatively high payload of more than 400 times its weight.

Although the research is at the initial state in regard to practical use, we believe that the proposed concept has high potential to be a new type of airless tire based on origami-inspired deformable structure. We expect that this new type of tire can be applied to various wheeled applications that require high mobility from a home service robot to a personal mobility. There can be three barriers in expanding the application fields of this concept—deformation ratio, size limitation, and maximum payload.

The first topic is about the deformation ratio. The proposed design used the identical repeated unit pattern and the repetition number is fixed by 3×8. Under these conditions, it was possible to find the optimal design parameter for the deformation ratio based on the kinematic analysis. Increasing the repetition number of the pattern will increase the maximum diameter of the wheel without change of the minimum diameter, but it could make the structure more pliable by providing additional freedom. Changing the shape of the unit pattern is also an interesting issue for improving the performance of the wheel. The square unit pattern can be replaced by rectangle or parallelogram. The variation of the unit pattern shape will allow the hub, support, and rim part to have their own functional design.

The second topic is about the size limitation. Origami structure is basically scalable because of a frictionless joint, which is one of the important advantages of origami-based mechanism. The proposed wheel, however, has multiple stacking folding part and is also composed of multi-material. The size limitation comes from material thickness and dissimilar material bonding. The thickness of the facet used in this research is about 100 μm, which is ignorable compared to the length of the facet, but the scale down of the wheel without a change of material thickness will cause a collision between adjacent facets. The scale up of the wheel has a problem on dissimilar material adhesion. The adhesive force between the fold line layer with the facet layer is an important factor for maximum payload. However, load is increased by a cubic, while adhesive force is increased by a square, and this discrepancy causes a problem. This topic will be discussed in more detail with a payload issue.

The third topic is about the payload. Expanding the range of material selection for the facet and the fold line is an essential requirement for increasing the payload. In this research, a combination of PET and mesh fabric is used, but there are a variety of options for material selection, including carbon reinforced plastic plate, polycarbonate, ABS resin for the facet, and special purpose fabric such as aramid fiber,

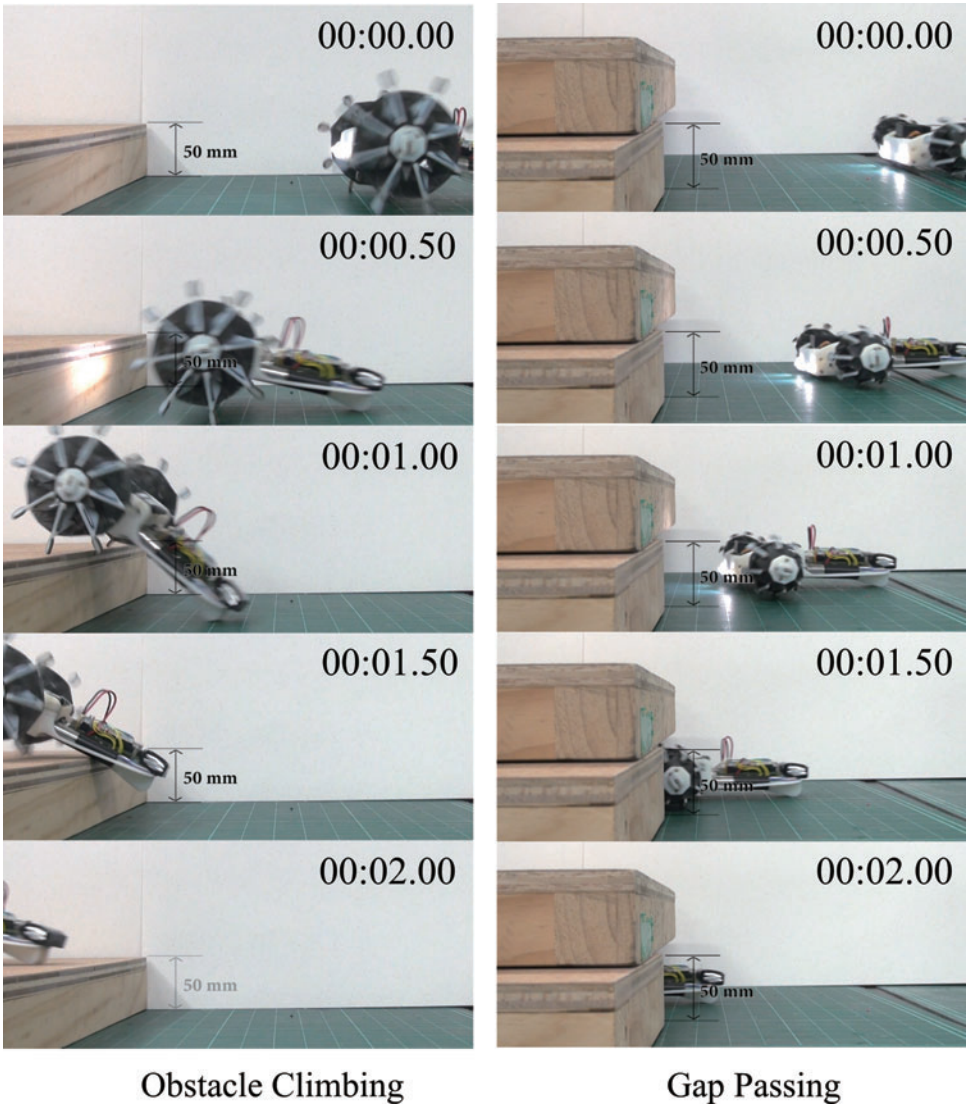

FIG. 23. Video snapshots of the maneuverability performance test. The video file is available in Supplementary Video S1 (Supplementary Data are available online at www.liebertpub.com/soro). Color images available online at www.liebertpub.com/soro

Kevlar, for the fold line layer. The important question is how to pattern, align, and adhere these materials.

Accurate pattern alignment is critical to maintaining the payload performance consistency. The weak adhesive film was used for the pattern alignment in this research, but this method should be diversified depending on the material. Using a replaceable jig or a soluble dummy plot can be a candidate. Because the collapse of the wheel is mainly caused by two reasons, material failure and delamination, the adhesive force is also an important factor for payload performance. In this research, the porosity of the mesh fabric increases adhesive force, but it cannot completely prevent the delamination. We will explore better adhesive methods such as plasma etching, welding, sewing, and mechanical locking.

Increasing the thickness of the material is a way to increase a payload without material change. However, to be folded compactly, a thicker material requires a larger fold line region and it increases the pliability of the structure. In addition, increasing the thickness requires a larger force to deform the wheel. The effect of these conflicting factors is difficult to be analyzed by the kinematic model. The study on this issue needs to be addressed by finite element analysis.

Prediction of the effective stiffness and maximum payload of the wheel according to the material properties of the facets and folding parts is important for material selection and design optimization. The kinematic model allows the optimization of the deformation ratio and ensures that the structure has necessary degrees of freedom, but the stiffness and payload of the wheel cannot be predicted because of the unpredictable behavior of the facets, including the flexible facet regions. Similar to the thickness problem, the structure analysis based on finite element method is required to address this issue.

The last topic is the hybrid patterning. We think that hybrid patterning is one of the unique advantages of the combination of soft robotic design approach with origami-inspired design approach. For our wheel application, most of the parts were patterned, and only two types of facets were used. Local patterning with various types of facets can provide various additional functionalities. For example, some regions can be given highly flexibility, while others can be constrained. Facets with appropriate compliance can be used as spring components, not just as rigid components. This design approach could be accomplished not only by varying the materials

used but also by applying specific hole patternings. We will investigate this in future work. Balancing the degrees of freedoms and constraints of origami structures will enlarge the application field of soft robotics.

Acknowledgments

This material is based on work supported by the ICT R&D program of MSIP/IITP (R0190-15-2040, Development of a content configuration management system and a simulator for 3D printing using smart materials), the National Research Foundation of Korea (NRF) Grant funded by the Korean Government (MSIP) (No. NRF-2016R1A5A1938472), and the Air Force Office of Scientific Research under award number FA2386-16-1-4052.

Author Disclosure Statement

No competing financial interests exist.

References

1. Chen S-C, Huang K-J, Chen W-H, Shen S-Y, Li C-H, Lin P-C. Quattroped: a leg—wheel transformable robot. IEEE/ASME Trans Mechatronics 2014;19:730–742.
2. Kim Y-S, Jung G-P, Kim H, Cho K-J, Chu C-N. Wheel transformer: a wheel-leg hybrid robot with passive transformable wheels. IEEE Trans Robotics 2014;30:1487–1498.
3. Nagatani K, Kuze M, Yoshida K. Development of transformable mobile robot with mechanism of variable wheel diameter. J Robotics Mechatronics 2007;19:252–257.
4. She Y, Hurd CJ, Su HJ. A transformable wheel robot with a passive leg. IEEE/RSJ Int Conf Intelligent Robots Syst 2015:4165–4170.
5. Ilievski F, Mazzeo AD, Shepherd RF, Chen X, Whitesides GM. Soft robotics for chemists. Angew Chem Int Ed Engl 2011;50:1890–1895.
6. Kim S, Laschi C, Trimmer B. Soft robotics: a bioinspired evolution in robotics. Trends Biotechnol 2013;31:287–294.
7. Majidi C. Soft robotics: a perspective—current trends and prospects for the future. Soft Robotics 2013;1:5–11.
8. Shepherd RF, Ilievski F, Choi W, Morin SA, Stokes AA, Mazzeo AD, Chen X, Wang M, Whitesides GM. Multigait soft robot. Proc Nat Acad Sci 2011;108:20400–20403.
9. Loepfe M, Schumacher CM, Lustenberger B, Stark WJ. An untethered, jumping roly-poly soft robot driven by combustion. Soft Robotics 2015;2:33–41.
10. Waynelovich J, Frey T, Baljon A, Salamon P. Versatile and dexterous soft robotic leg system for untethered operations. Soft Robotics 2016;3:64–70.
11. Lang RJ. The science of origami. Phys World 2007;20:30.
12. Dureisseix D. An overview of mechanisms and patterns with origami. Int J Space Struct 2012;27:1–14.
13. Felton S, Tolley M, Demaine E, Rus D, Wood R. A method for building self-folding machines. Science 2014;345:644–646.
14. Peraza-Hernandez EA, Hartl DJ, Malak RJ, Lagoudas DC. Origami-inspired active structures: a synthesis and review. Smart Mat Struct 2014;23:094001.
15. Martinez RV, Fish CR, Chen X, Whitesides GM. Elastomeric origami: programmable paper-elastomer composites as pneumatic actuators. Adv Funct Mater 2012;22:1376–1384.
16. Lee D-Y, Koh J-S, Kim J-S, Kim S-W, Cho K-J. Deformable-wheel robot based on soft material. Int J Precision Eng Manuf 2013;14:1439–1445.
17. Lee D-Y, Jung G-P, Sin M-K, Ahn S-H, Cho K-J. Deformable wheel robot based on origami structure. IEEE Int Conf Robotics Automat 2013:5612–5617.
18. Lee D-Y, Kim J-S, Kim S-R, Koh J-S, Cho K-J. The deformable wheel robot using magic-ball origami structure. ASME Int Design Eng Techn Conf 2013:V06BT07A040.
19. Lee D-Y, Kim J-S, Park J-J, Kim S-R, Cho K-J. Fabrication of origami wheel using pattern embedded fabric and its application to a deformable mobile robot. IEEE Int Conf Robotics Automat 2014:2565
20. Lee J-Y, Kang BB, Lee D-Y, Baek S-M, Kim W-B, Choi W-Y, *et al.* Development of a multi-functional soft robot (SNUMAX) and performance in RoboSoft Grand Challenge. Front Robotics AI 2016;3:63.
21. Kuribayashi K, Tsuchiya K, You Z, Tomus D, Umemoto M, Ito T, *et al.* Self-deployable origami stent grafts as a biomedical application of Ni-rich TiNi shape memory alloy foil. Mat Sci Eng 2006;419:131–137.
22. Le PH, Wang Z, Hirai S. Origami structure toward floating aerial robot. IEEE Int Conf Adv Intellig Mechatronics 2015:1565–1569.
23. Ma J, You Z. Modelling of the waterbomb origami pattern and its applications. ASME Int Design Eng Techn Conf 2014:V05BT08A047.

Address correspondence to:
Kyu-Jin Cho
Department of Mechanical and Aerospace Engineering
Seoul National University
Gwanak-ro, Gwanak-gu, Seoul 151-742
Korea

E-mail: kjcho@snu.ac.kr